RESEARCH ARTICLE

Pancam Multispectral Imaging Results from the Spirit Rover at Gusev Crater

J. F. Bell III,[1]* S. W. Squyres,[1] R. E. Arvidson,[2] H. M. Arneson,[1] D. Bass,[3] D. Blaney,[3] N. Cabrol,[4] W. Calvin,[5] J. Farmer,[6] W. H. Farrand,[7] W. Goetz,[8] M. Golombek,[3] J. A. Grant,[9] R. Greeley,[6] E. Guinness,[2] A. G. Hayes,[1] M. Y. H. Hubbard,[1] K. E. Herkenhoff,[10] M. J. Johnson,[1] J. R. Johnson,[10] J. Joseph,[1] K. M. Kinch,[11] M. T. Lemmon,[12] R. Li,[13] M. B. Madsen,[8] J. N. Maki,[3] M. Malin,[14] E. McCartney,[1] S. McLennan,[15] H. Y. McSween Jr.,[16] D. W. Ming,[17] J. E. Moersch,[16] R. V. Morris,[17] E. Z. Noe Dobrea,[1] T. J. Parker,[3] J. Proton,[1] J. W. Rice Jr.,[6] F. Seelos,[2] J. Soderblom,[1] L. A. Soderblom,[10] J. N. Sohl-Dickstein,[1] R. J. Sullivan,[1] M. J. Wolff,[7] A. Wang[2]

Panoramic Camera images at Gusev crater reveal a rock-strewn surface interspersed with high- to moderate-albedo fine-grained deposits occurring in part as drifts or in small circular swales or hollows. Optically thick coatings of fine-grained ferric iron–rich dust dominate most bright soil and rock surfaces. Spectra of some darker rock surfaces and rock regions exposed by brushing or grinding show near-infrared spectral signatures consistent with the presence of mafic silicates such as pyroxene or olivine. Atmospheric observations show a steady decline in dust opacity during the mission, and astronomical observations captured solar transits by the martian moons, Phobos and Deimos, as well as a view of Earth from the martian surface.

On 4 January 2004 universal time coordinated, the Mars Exploration Rover, Spirit, landed on Mars at 14.5692°S, 175.4729°E, within the crater Gusev, a 160-km-diameter Noachian-age impact crater. Previous orbital remote sensing data have been used to hypothesize that Gusev crater may be partially infilled by ancient lacustrine sediments (*1*, *2*). We acquired high spatial resolution multispectral panoramic images of the landing site and its environs to characterize the morphology, composition, and physical and atmospheric properties of the region. Our primary objective is to relate these characteristics to the origin and evolution of the martian crust, with particular emphasis on the search for evidence of liquid water in this region in the past.

Instrumentation and calibration. Panoramic Camera (Pancam) is a digital imaging system consisting of two 1024 pixel by 1024 pixel charge-coupled device (CCD) cameras with a 30-cm stereo separation and 0.27 mrad per pixel resolution, mounted on a mast assembly ~1.5 m above the martian surface (*3*). Each camera has an eight-position filter wheel and is capable of obtaining narrow-band color images of the surface or sky in 11 distinct narrow bands or direct neutral-density filter images of the Sun for opacity determinations at two wavelengths. Because of downlink bandwidth limitations, most images were compressed before downlink with the use of a

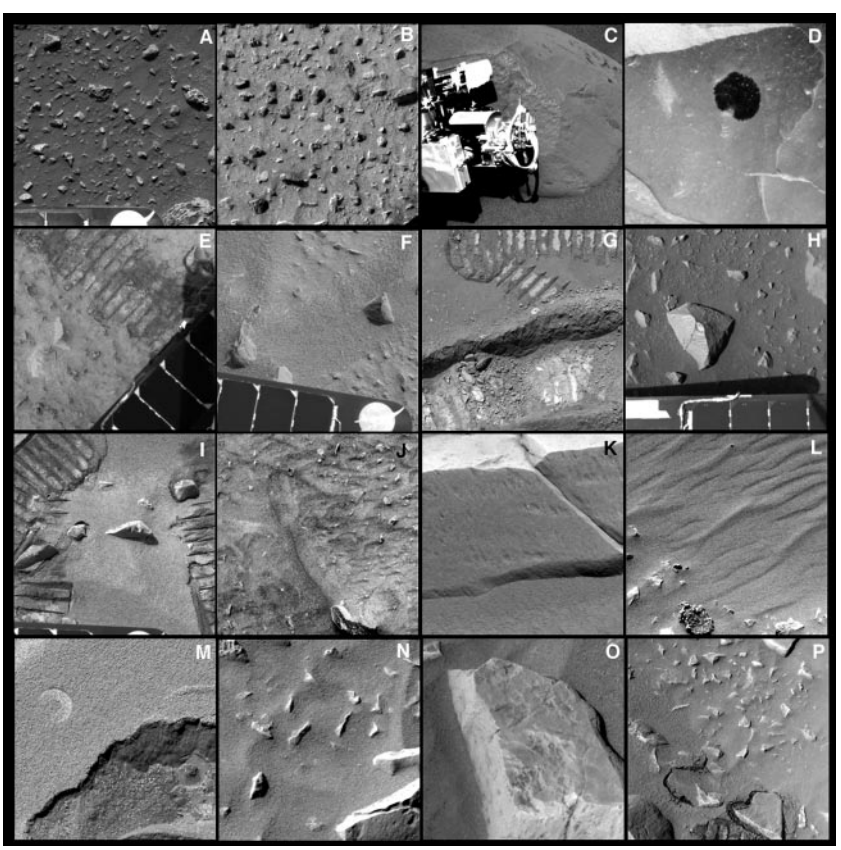

Fig. 1. Close-up of examples of rocks, clasts, and fine-grained deposits in the region directly in front of the rover (at Pancam's highest resolution). The features are ~1.6 m from the camera, and each image is about 40 to 50 cm across, The smallest features visible in the images are ~0.8 to 1.0 mm across. (**A**) Sol 12, sequence P2269, filter L7 (430 nm). (**B**) Sol 12, sequence P2269, filter L2 (754 nm). (**C**) Sol 30, sequence P2558, filter L7 (430 nm). (**D**) Sol 33, sequence P2563, filter L2 (754 nm). (**E**) Sol 36, sequence P2282, filter L2 (754 nm). (**F**) Sol 39, sequence P2593, filter L2 (754 nm). (**G**) Sol 50, sequence P2420, filter L7 (430 nm); (**H**) Sol 50, sequence P2566, filter R1 (430 nm). (**I**) Sol 51, sequence P2425, filter L2 (754 nm). (**J**) Sol 54, sequence P2581, filter L2 (754 nm). (**K**) Sol 63, sequence P2530, filter R1 (430 nm). (**L**) Sol 66, sequence P2514, filter R1 (430 nm). (**M**) Sol 74, sequence P2560, filter L7 (430 nm). (**N**) Sol 75, sequence P2562, filter L7 (430 nm). (**O**) Sol 76, sequence P2566, filter R1 (430 nm). (**P**) Sol 90, sequence P2514, filter R1 (430 nm).

high-quality but lossy wavelet-based compression algorithm (*4*). Bandwidth and power limitations also forced many multispectral observations to be acquired with the use of only a subset (typically 5 or 6) of the 13 narrow-band surface filters.

Calibration was achieved through a combination of preflight laboratory measurements and daily measurements of an onboard reflectance calibration target (*3*). The calibration target was observed to gradually redden over time because of the accumulation of

[1]Cornell University, Ithaca, NY 14853–6801, USA. [2]Washington University, St. Louis, MO 63130, USA. [3]Jet Propulsion Laboratory–California Institute of Technology, Pasadena, CA 91109, USA. [4]National Aeronautics and Space Administration (NASA) Ames Research Center–Search for Extraterrestrial Intelligence Institute, Moffett Field, CA 94035, USA. [5]University of Nevada, Reno, NV 89501, USA. [6]Arizona State University, Tempe, AZ 85287, USA. [7]Space Science Institute, Boulder, CO 80301, USA. [8]University of Copenhagen, DK-2100 Copenhagen Ø, Denmark. [9]National Air and Space Museum, Washington, DC 20560, USA. [10]U.S. Geological Survey, Flagstaff, AZ 86001, USA. [11]Aarhus University, DK-8000 Aarhus C, Denmark. [12]Texas A&M University, College Station, TX 77843, USA. [13]Ohio State University, Columbus, OH 43210, USA. [14]Malin Space Science Systems, Incorporated, San Diego, CA 92191, USA. [15]State University of New York at Stony Brook, Stony Brook, NY 11794, USA. [16]University of Tennessee, Knoxville, TN 37996, USA. [17]NASA Johnson Space Center, Houston, TX 77058, USA.

*To whom correspondence should be addressed. E-mail: jfb8@cornell.edu

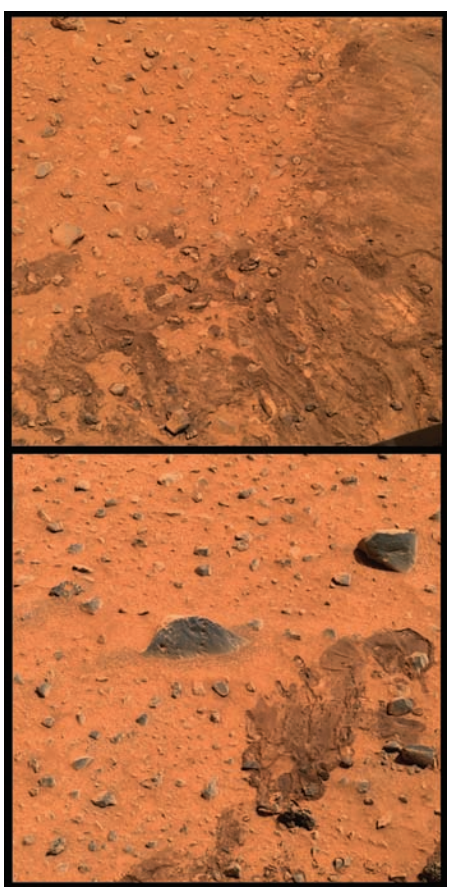

Fig. 2. Examples of gravel armor and crusted fines observed in Pancam images of airbag scape marks near the lander. (**Top**) Sol 11, sequence P2536, 10:45 local solar time (LST); (**bottom**) sol 7, sequence P2530, 13:20 LST. Both images are approximate true color renderings generated with the use of Pancam's 600 nm, 530 nm, and 480 nm filters.

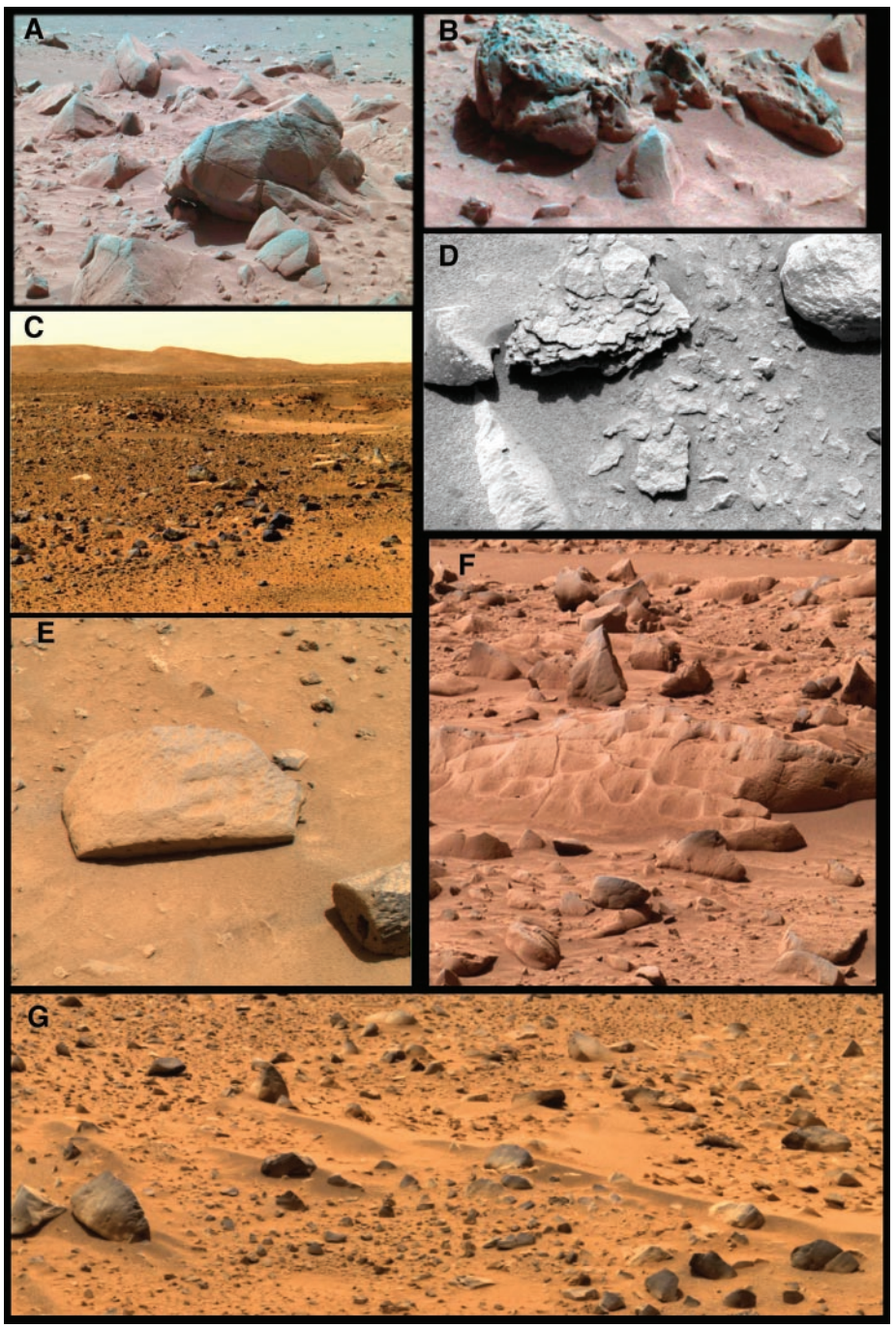

Fig. 3. Examples of the variety of rock forms observed by Pancam at the Gusev site. (**A**) A 77-cm-wide fractured block from sol 68 imaging near the rim of Bonneville crater. (**B**) A 25-cm-wide rock (left of frame) also imaged on sol 68, showing both vesicular and smooth morphologies. (**C**) Sol 49 view of the boundary between Laguna Hollow (near field) and the surrounding plains, showing typical increased rock abundance near the periphery of the hollow. (**D**) Image of the 5-cm-wide platy rock Mimi from sol 42. (**E**) The rocks Sashimi (center, 30 cm long, and 18 cm wide) and Sushi (lower right, 10 cm wide) imaged near the lander on sol 14. Sashimi is moderately pitted and exhibits ventifact-like aeolian scour marks; Sushi is heavily pitted, including a large angular pit in the exposed interior of the left side of the rock. (**F**) The low-lying rock Mazatzal, imaged on sol 76. The rock is ~2.1 m long and ~ 45 cm high. (**G**) View from sol 5 of small rocks and aeolian bedforms near the lander, showing that the most rounded-looking rocks near the lander are also typically the darkest. The small rock next to the bedform at center is ~15 cm across.

settling airborne dust on its surface. The degree of reddening and its influence on the image calibration has been modeled with the use of a simple two-layer Hapke model of a thin layer of dust with spectral properties like those determined by the Viking and Pathfinder landers (*5*–*7*) on top of the silicone-based calibration target materials (*3*). The model was verified and validated by using results from the Sweep Magnet experiment (*8*). With this time-variable dust correction applied, the cameras' absolute radiance calibration is estimated to be within ~5 to 10% accuracy on the basis of comparison with sky radiance models and direct imaging of the Sun (*9*, *10*). The relative reflectance (radiance factor or I/F, where I is the measured scene radiance and πF is the solar irradiance at the top of the martian atmosphere) is estimated to be within ~5 to 10% absolute accuracy and ~1 to 3% relative filter-to-filter precision.

During the course of Spirit's 90-sol (*11*) primary mission, more than 9300 Pancam images, totaling more than 750 Mbytes of data, were acquired and downlinked. Among these images were sets of large multispectral panoramas acquired from the initial landing site, from halfway along the traverse to a nearby crater informally known as Bonneville (*12*), and from the rim of Bonneville itself. These panoramas were acquired with the use of a subset of Pancam filters designed to provide stereo coverage, span the full wavelength range of the instrument, and cover key wavelengths that could provide tactical time scale information on potential drive directions and/or in situ instrument target choices.

Regional-scale observations. The panoramic views of the landing site and traversed regions (Plates 1 to 3) show a generally flat plain with about 5% of the area covered by relatively small (tens of cm size or smaller) rocks. Most of the rocks are angular to subangular, and a small number are rounded. The 210-m-diameter rim of Bonneville crater could be seen about 300 m northeast of the lander. More distant features include a ridge of low-lying (~100 to 150 m high) hills, called the Columbia Hills (Plate 4), ~3 to 4 km east of the lander and isolated knobs and mesas ranging from ~8 km to ~26 km south to southwest of the lander near the mouth of Ma'adim Vallis. There were more rocks on the Bonneville crater ejecta blanket, with ~10% of the area covered by rocks (*13*, *14*). The local relief around the landing site exhibits meter-scale undulations interspersed with small (< 200-m diameter), low-relief (< 15-m depth) impact craters and much smaller (tens of m in diameter) circular hollows. Full resolution, losslessly compressed Pancam images reveal morphologic, albedo, and color variations within the Columbia Hills that may indicate scarps, terraces, or layers such as those identified in Mars Global Surveyor (MGS) Mars Orbiter Camera images (*1*, *2*, *15*).

Rocks and fines. Clastic materials imaged by Pancam at the landing site encompass a range of morphologies and physical properties (Fig. 1). Examples of fines include thin reddish aeolian dust coatings, fine-grained soil particles (*16*), sand, granules, and gravel. Bedforms hypothesized to be ripples formed of coarse sand and granules ~0.5 to several mm in size were identified on the basis of Pancam albedo and color variations; this hypothesis was verified with the use of Microscopic Imager (MI) images (*17*, *18*). Most fines observed at the landing site show some cohesion on the basis of how the material holds together when disturbed by the rover wheels, airbag bounces, and drag marks or the Mössbauer spectrometer contact plate (*18*). There is also some evidence for layering of finer-grained materials above and below an armor of what appear to be gravel, pebbles, and cobbles (Fig. 2). The coarser layers may have formed by accretion of aeolian fine-grained dust on the basis of images from regions where larger particles are not seen beneath the surface (e.g., Plate 7), or they may represent deflational lag deposits on the basis of images from other regions where larger particles are seen beneath the surface [e.g., within trenches or the Serpent bedform (*18*, *19*)].

Many rocks at the landing site are fractured or fragmented, and some are pitted and may contain vesicles (Fig. 3). Some rocks are partially buried by fines, whereas others are perched on the surface. Rounded rocks are rare and are generally darker and display signs of wind erosion rather than any unambiguous indications of a fluvial origin. No sedimentary rocks or impact breccias have been identified at the site.

Photometric observations. Calibrated Pancam images from sequences acquired with the use of a broadband filter (L1, 739 ± 338 nm bandpass) were used to estimate the albedo of the landing site region to be 0.25 ± 0.05 (*20*). This is a moderately high albedo for Mars, comparable to the MGS Thermal Emission Spectrometer (TES) bolometric albedo of the Viking Lander 1 site (0.26 ± 0.05), slightly higher than the albedo of the Viking Lander 2 (0.23 ± 0.01) or the MPF (0.22 ± 0.01) sites but within the uncertainties of previous orbital and telescopic estimates of the albedo of the Gusev landing error ellipse [~0.23 (*17*)]. Some of the uncertainty on the Pancam albedo estimate comes from albedo variations visible in images of the landing site region. The lander itself is within a slightly lower–albedo

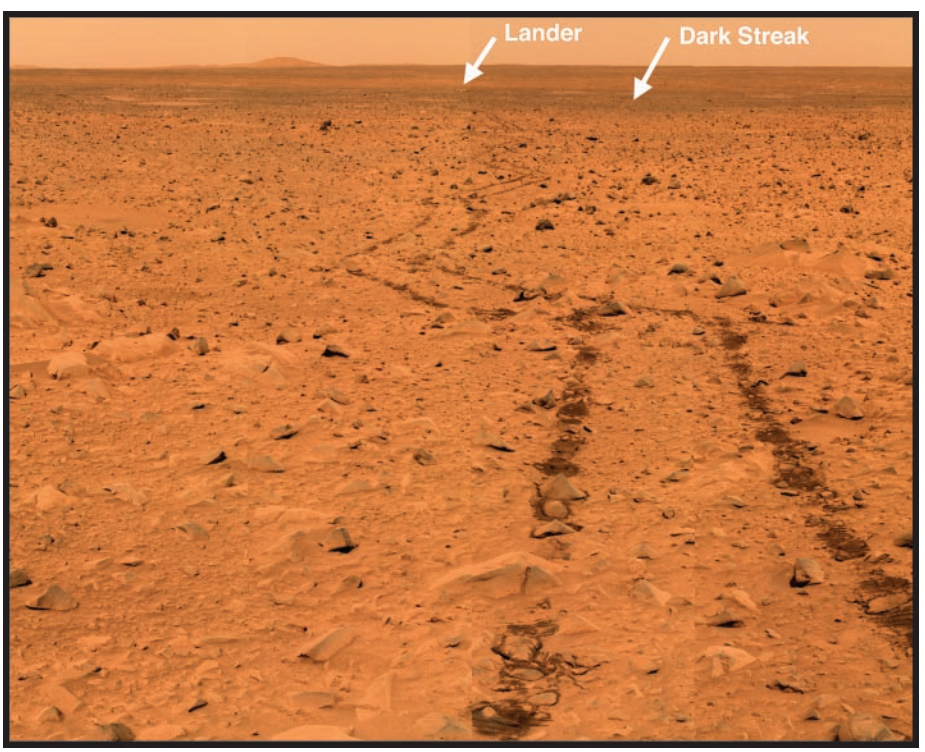

Fig. 4. Pancam mosaic acquired from near the rim of Bonneville crater, looking back to the southwest along the traverse path toward the lander (**center**, **top**). This view shows the lander to be within a wind or dust devil streak with a lower albedo than the more distant Gusev plains or the near-field crater ejecta deposit. This is an approximate true color rendering of a mosaic acquired around 10:20 LST on sol 66 with the use of Pancam's 750 nm, 530 nm, and 480 nm filters.

(0.20 ± 0.02) wind streak or dust devil track that trends northwest to southeast across the center of Gusev crater. During the first 90 sols, the rover crossed albedo boundaries associated with this lower-albedo wind streak and the higher-albedo (0.30 ± 0.02) hollows and the ejecta deposits of Bonneville crater (Fig. 4). These albedo extremes are consistent with the lowest (~0.19) and highest (~0.26) albedos measured by TES within the Gusev landing error ellipse (*14*).

Pancam multispectral images acquired at different times of day document reflectance variations related to surface properties such as texture, porosity, and grain size (*21*, *22*). For example, photometric observations of regions near the shadow cast by the Pancam mast assembly indicated a strong opposition effect in some soil and rock surfaces, and specular brightenings seen in some brushed and/or compacted surfaces suggest very fine-grained soils or smooth, reflective mineral surfaces in the rocks. Photometric observations were coordinated to occur during or within 1 sol of spacecraft overflights by the Mars Odyssey, Mars Express, and MGS orbiters to provide ground truth observations of visible and near-infrared (IR) reflectance as a function of illumination and viewing geometries.

Multispectral observations. The multispectral panoramas acquired from the Columbia Memorial Station and along Spirit's traverse (Plates 1 to 3) show broad classes of color units detectable at and near the landing site. For example, in the initial 360° mission success panorama (Plate 8), rocks or parts of rocks that are less dusty appear bluer than average, as do lower-albedo, possibly coarser-grained soils. A red/blue color ratio metric was often used to distinguish less dusty from more dusty rocks (none of the rocks were observed to be completely dust-free). The general spectral and color classes seen near the station include (i) high-albedo (0.25 to 0.35) red soils and drifts, (ii) moderate-albedo (0.20 to 0.25) red soils, such as those in the hollows, (iii) moderate- to high-albedo (0.20 to 0.30) red rock surfaces, (iv) moderate- to low-albedo (0.15 to 0.20) red drifts and far-field soils, (v) low-albedo (0.10 to 0.15) red disturbed soil deposits, and (vi) low-albedo (0.10 to 0.15) gray rock surfaces.

Less-compressed 13-filter (11-color) Pancam multispectral observations of selected targets provide additional constraints on the mineralogy associated with these spectral classes. Moderate- and high-albedo soil spectra (e.g., Figs. 5, A and B, and 6, A and B) are similar to telescopic and spacecraft measurements of martian dust (*14*, *23*, *24*) and are characteristic of fine-grained, poorly crystalline ferric iron oxides (*25*, *26*). A weak absorption centered near 860 to 930 nm in most high-albedo soil spectra can be used to constrain the ferric iron oxide mineralogy; however, a unique mineral identification cannot be assigned for this feature on the basis of Pancam data alone. Candidates to explain the near-IR band include fine-grained hematite, goethite, ferrihydrite, maghemite, or schwertmannite (*25*, *26*). The spectra of lower-

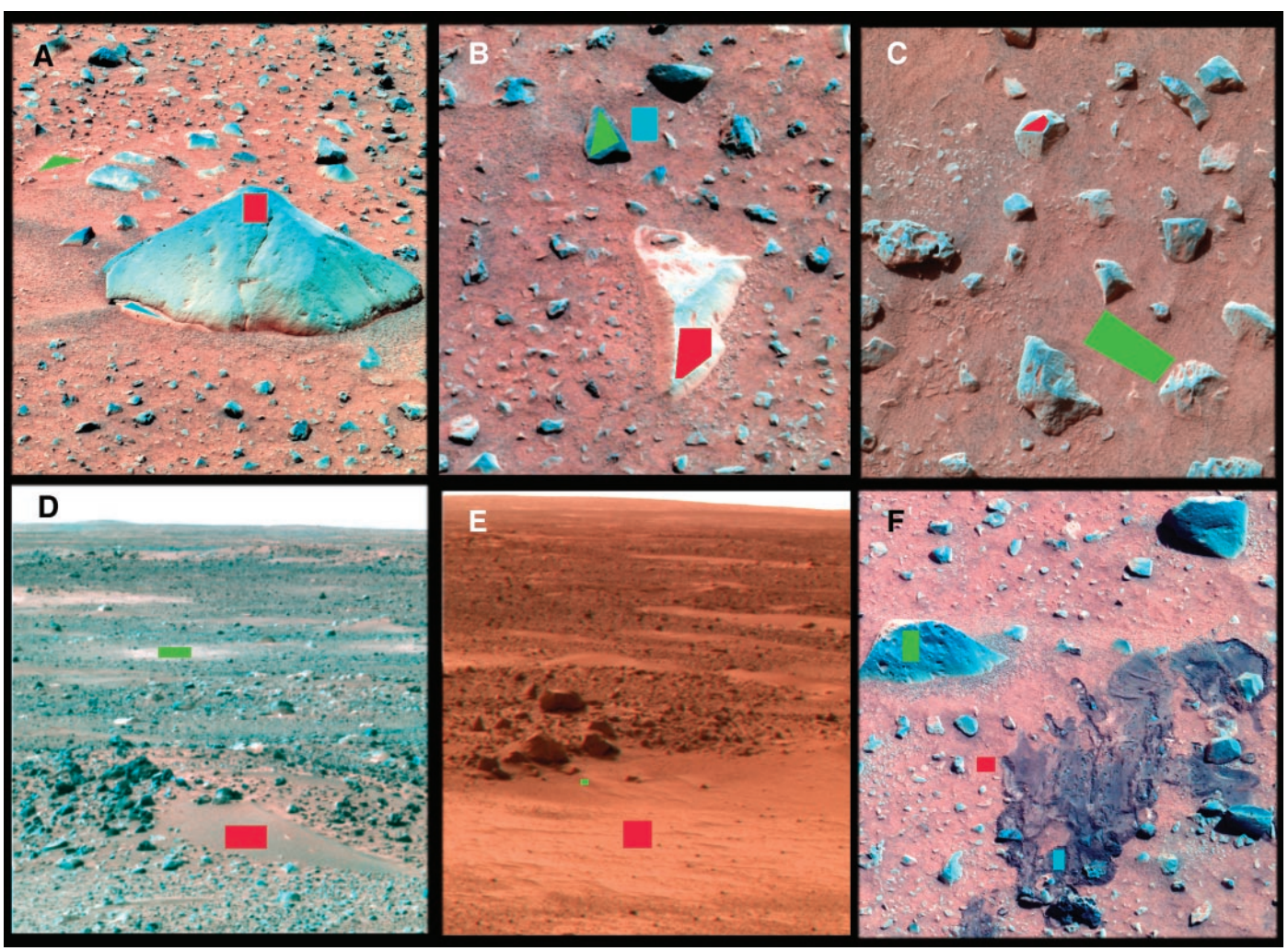

Fig. 5. Context images for Pancam spectra displayed in Fig. 6. All images are false-color composites using Pancam's 750 nm, 530 nm, and 480 nm filters. (**A**) Sol 14, target Adirondack; (**B**) sol 26, target Blanco; (**C**) sol 12, targets within the instrument arm work volume; (**D**) sol 9, position 1 within the 120 survey sequence; (**E**) sol 9, position 8 within the 120 survey sequence; and (**F**) sol 7, target Magic Carpet.

albedo undisturbed soils at the site (e.g., Figs. 5, D and F, and 6, D and F) can be modeled by a simple scaling of bright soil spectra, suggesting that the iron-bearing mineralogy of these regions is similar to that of the bright dust deposits but that the grain size of the materials is larger. Such a grain-size variation is also consistent with the interpretation of albedo boundaries seen on small aeolian ripple deposits at the site (*17*). Pancam images were also obtained of three different sets of magnets carried by Spirit that were designed to provide constraints on the composition and physical properties of magnetic dust grains (*27*). Initial results of the imaging and other measurements on the magnets indicates that essentially all of the airborne dust is magnetic and that the dust particles must be composite, multi-mineral-phase grains (*8*).

Pancam spectra of rock surfaces display a continuum of characteristics between light-toned red rock surfaces with spectra similar to bright soils (e.g., Figs. 5, A and B, and 6, A and B), likely indicating a fine-grained ferric iron oxide dust covering or coating, to much lower-albedo gray surfaces that are spectrally distinct (Figs. 3; 5, C and F; and 6, C and F). Specifically, the lowest albedo rock surfaces (naturally occurring or in regions of brushing and grinding) have a higher reflectance in the bluest wavelengths than the soils and dust, show an overall negative spectral slope from 750 nm to 1000 nm, and exhibit a weak near-IR absorption feature that is centered at a longer wavelength than the near-IR feature seen in the dust. These spectral characteristics are consistent with a lower relative percentage of ferric iron phases (less dust and/or soil cover) in these parts of the rocks and with ferrous iron silicates such as pyroxene or olivine to explain the longer-wavelength near-IR band (*28*–*33*). These spectral characteristics are also consistent with the Mössbauer spectrometer observations of rock surfaces (*34*, *35*), and similar spectral characteristics were observed in a rare "black rock" spectral class of materials at the MPF landing site (*33*).

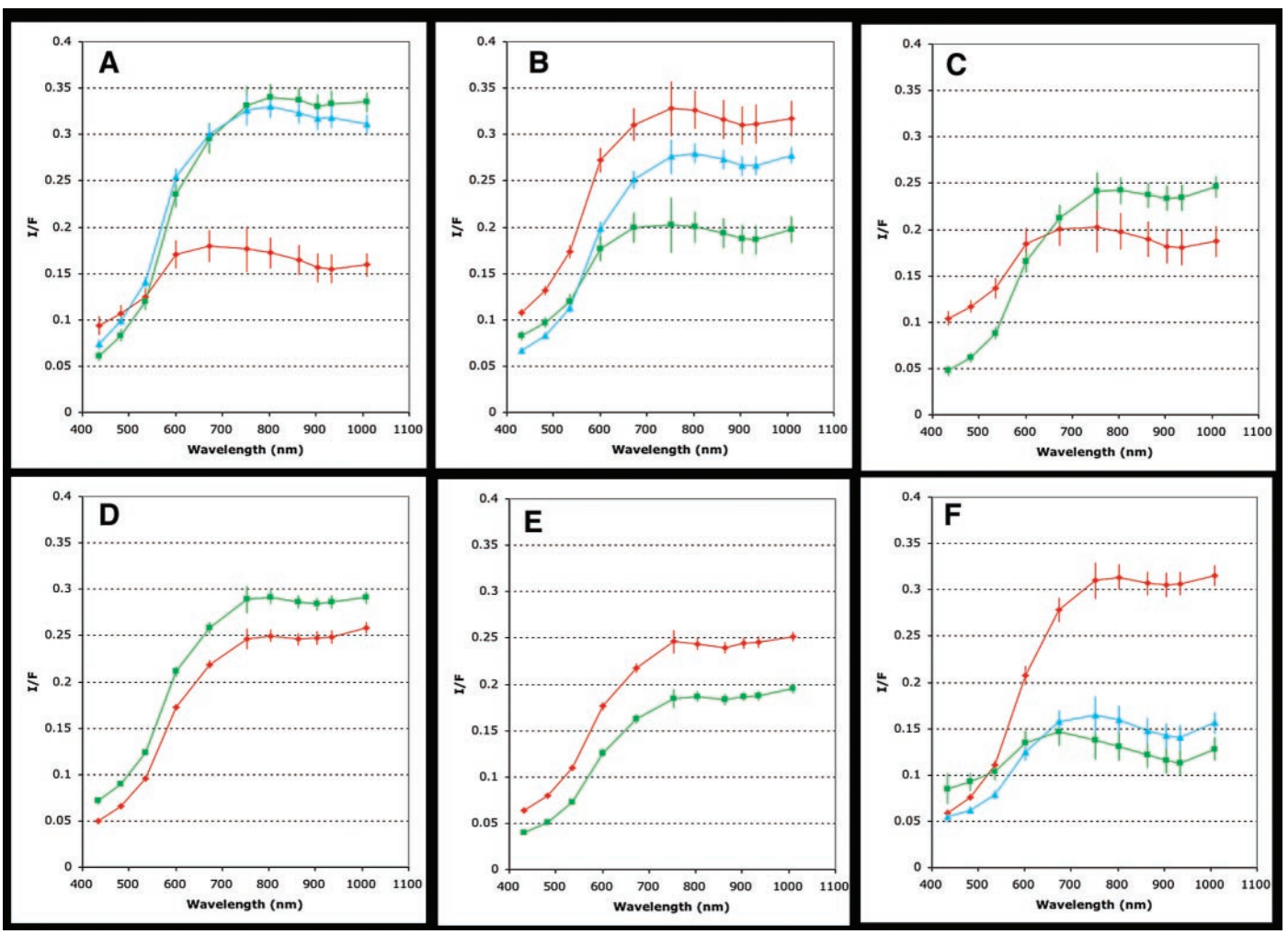

Fig. 6. Thirteen-filter Pancam spectra showing the range of spectral diversity seen within rocks and soils at the Gusev site. Each colored spectrum comes from the region of interest of the same color in the corresponding frame of Fig. 5. No corrections for local topography effects (incidence angle variations) are included in these spectra.

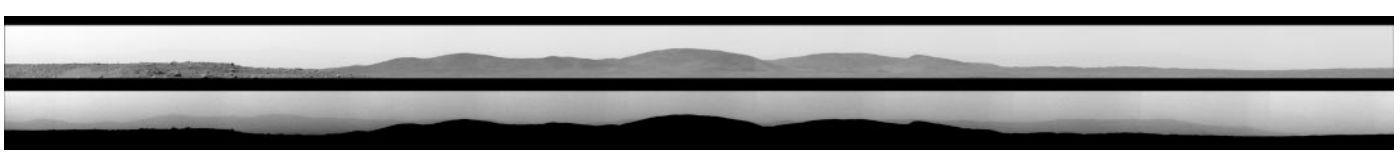

Fig. 7. Pancam panorama from sol 85, sequence P2365, blue filter (430 nm). (**Top**) The Columbia Hills are prominent "foreground" objects ~3 km from the rover. (**Bottom**) With a harsher contrast enhancement, the rim of Gusev crater, ~80 km from the rover, can be seen in the distance.

Pancam images and spectra of soils that were disturbed by the airbags or during trenching activities (Figs. 5F and 6F and Plate 7) reveal low-albedo materials that have more in common spectrally with dark rock surfaces than with dark soils. Specifically, the lower albedo, lower red/blue ratio, stronger near-IR spectral slope, and deeper near-IR absorption feature are consistent with a lower Fe^{3+}/Fe^{2+} ratio in the disturbed soils relative to undisturbed soils. The Pancam spectral data from the trench that was dug in Laguna Hollow (*19*) (Plate 7) show that the uppermost more oxidized (ferric iron–rich) layer of the soil in the hollow is quite thin, because this dust-like spectral signature is not seen in the spectra of the walls or the floor of the trench. This result is also consistent with Mössbauer spectra of the trench (*34*, *35*), which showed the surface soils to be more oxidized than the trench interior. The dusty soils may have an even higher Fe^{3+}/Fe^{2+} ratio than inferred from the Mössbauer data, because the surface observed by Pancam (the upper few micrometers of the surface) is much thinner than the Mössbauer penetration depth.

Fig. 8. Navcam presunrise image of the eastern horizon and sky, acquired at 04:47 LST on sol 63, with an overlaid Pancam image of the Earth acquired a few minutes later with the use of the broadband L1 filter. The Earth is the faint "star" in the center of the frame.

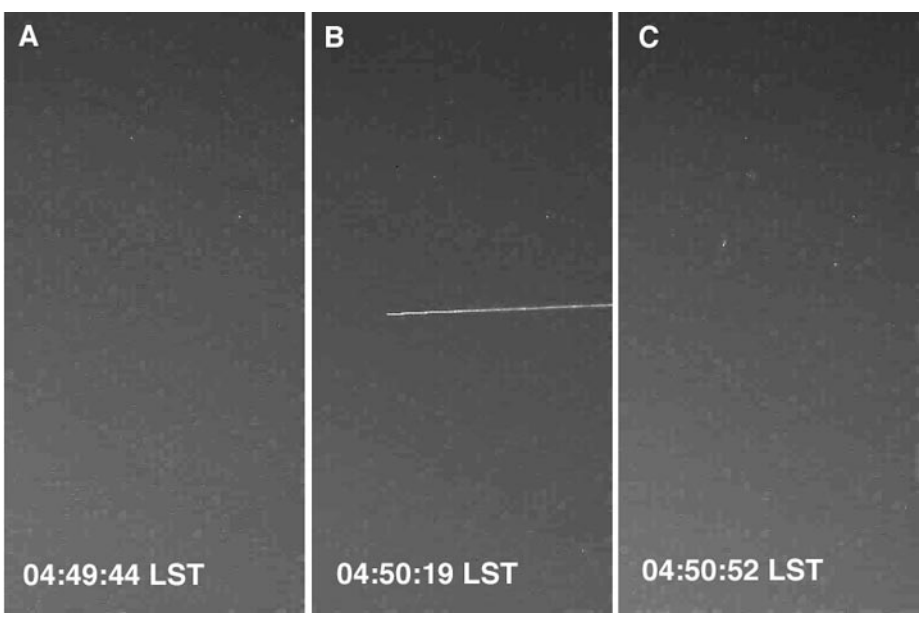

Fig. 9. Three sequential raw Pancam images acquired as part of the Earth-imaging sequence on sol 63. (**A**) Image 2P131930902ESF1300P2733L4M1, acquired at 04:49:44 LST. (**B**) Image 2P131930937ESF1300P2733L5M1, acquired at 04:50:19 LST and showing an anomalously bright streak that may be a meteor trail. (**C**) Image 2P131930972ESF1300P2733L6M1, acquired at 04:50:52 LST. All three images were pointed at the same region of the sky and had an exposure time of 15 s.

Three of the rocks that were studied in detail with the in situ instruments included a small two-toned angular rock near the lander named Adirondack (Plate 9), a large partly dust-covered rock halfway along the traverse to Bonneville named Humphrey (Plate 10), and a long but low-lying light-toned rock named Mazatzal along the traverse near the rim of Bonneville (Plate 11). Pancam images of these rocks were used to select MI, Mössbauer, α particle x-ray spectrometer (APXS), and Rock Abrasion Tool (RAT) target regions on the basis of both morphologic and color considerations. Brushing and grinding into each of these rocks removed the bright red dust covering and any light-toned coatings and revealed their intrinsic gray color and near-IR spectral properties to be consistent with the presence of ferrous iron minerals such as pyroxene, olivine, and magnetite (*19*, *28*). The Pancam data on these freshly exposed rock interiors are consistent with the APXS, Mössbauer, and Mini-TES results, which indicate that these rocks are all olivine-bearing basalts (*28*, *33*, *35*) and that the light-toned veins seen in MI images of freshly exposed rock interiors are not simply fractures filled with reddish dust (Plates 12 and 13).

Atmospheric and astronomical observations. Daily (or many times daily) images of the Sun were obtained with the use of 440-nm and 880-nm neutral density filters in order to derive and monitor atmospheric dust opacity. The visible wavelength dust opacity at the start of the mission was ~0.9, a relatively high value that was likely related to enhanced global-scale dust storm activity that occurred during November and December 2003. By sol 90, the opacity had fallen to ~0.5 (*10*, *36*). The atmosphere had cleared enough by sol 85 to allow Pancam imaging of the walls of Gusev crater, some 80 km from the landing site (Fig. 7). Time-lapse observations of sunrise and sunset were also acquired in order to

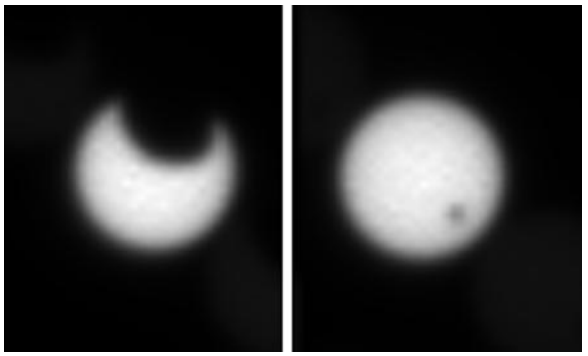

Fig. 10. Pancam solar filter images of Phobos and Deimos in midtransit. (**Left**) Phobos event observed on sol 104 (18 April 2004); (**right**) Deimos event observed on sol 68 (13 March 2004).

derive and monitor the vertical extent of dust in the atmosphere and to search for evidence of morning or evening twilight water ice clouds that are expected to begin forming as southern fall transitions into winter (*37*). During one of the cloud search sequences on sol 63, the Earth was observed in the presunrise twilight sky (Fig. 8). During that same imaging sequence, a long, anomalously bright streak was observed in one long-exposure Pancam image (Fig. 9). The streak's orientation is not consistent with the known or inferred paths of any Mars-orbiting spacecraft except perhaps Viking Orbiter 2, and thus the streak may represent a lucky observation of a meteor trail (*38*). Daytime sky observations and nighttime astronomical observations of stars and Deimos were acquired to search for evidence of clouds. As of the end of the primary mission (areocentric longitude of the Sun $\sim$ 15°, corresponding to early southern hemisphere autumn), no unambiguous clouds were detected at the landing site in Gusev, nor had any dust devils been detected either in dedicated dust devil search sequences or in serendipitous horizon imaging.

Lastly, Spirit's near-equatorial landing latitude made it possible to observe solar transits by the martian moons. Two transits were captured by Pancam from the Gusev site: one set of images of Deimos passing across the solar disk on sol 68 and one grazing Phobos transit event on sol 104 (Fig. 10) (*39*). Discrepancies between the predicted transit contact times and phase angles and those that were observed are being used to update the orbital ephemeris parameters of both satellites (neither of which have been carefully monitored in decades) (*40*). These calculations will provide dynamical information on the satellites' orbital evolutions as well as increased accuracy for future spacecraft imaging of the moons (*42*).

References and Notes

1. M. P. Golombek *et al.*, *J. Geophys. Res.* **108**, 10.1029/2003JE002074 (2003).
2. N. Cabrol *et al.*, *J. Geophys. Res.* **108,** 10.1029/2002JE002026 (2003).
3. J. F. Bell III *et al.*, *J. Geophys. Res.* **108**, 10.1029/2003JE002070 (2003).
4. J. N. Maki *et al.*, *J. Geophys. Res.* **108**, 10.1029/2003JE002077 (2003).
5. M. E. Ockert-Bell *et al.*, *J. Geophys. Res.* **102**, 9039 (1997).
6. J. F. Bell III *et al.*, *J. Geophys. Res.* **105**, 1721 (2000).
7. J. R. Johnson *et al.*, *Icarus* **163**, 330 (2003).
8. P. Bertelsen *et al.*, *Science* **305**, 827 (2004).
9. M. T. Lemmon, personal communication.
10. M. J. Wolff, Athena Science Team, *Proc. Lunar Planet. Sci.* **XXXV**, abstr. 2171 (2004) [CD].
11. A martian solar day has a mean period of 24 hours 39 min 35.244 s and is referred to as a sol to distinguish this from a roughly 3%-shorter solar day on Earth. A martian sidereal day, as measured with respect to the fixed stars, is 24 hours 37 min 22.663 s, as compared with 23 hours 56 min 04.0905 s for Earth. See http://www.giss.nasa.gov/tools/mars24/ for more information.
12. Names have been assigned to areographic features by the Mars Exploration Rover (MER) team for planning and operations purposes. The names are not formally recognized by the International Astronomical Union.
13. J. A. Grant *et al.*, *Science* **305**, 807 (2004).
14. M. Golombek *et al.*, *Lunar Planet. Sci.* **XXXV**, abstr. 2185 (2004) [CD].
15. M. C. Malin, Athena Science Team, *Lunar Planet. Sci.* **XXXV**, abstr. 2170 (2004) [CD].
16. The term martian soil is used here to denote any loose unconsolidated materials that can be distinguished from rocks, bedrock, or strongly cohesive sediments. No implication of the presence or absence of organic materials or living matter is intended [see, for example, (*6*)].
17. R. Greeley *et al.*, *Science* **305**, 810 (2004).
18. K. E. Herkenhoff *et al.*, *Science* **305**, 824 (2004).
19. R. E. Arvidson *et al.*, *Science* **305**, 821 (2004).
20. An estimated albedo is derived by dividing the *I/F* determined from observations calibrated with the onboard calibration target by the cosine of the solar elevation angle at the time of each observation. This albedo estimate should be comparable to the bolometric Lambert albedo values derived from orbital observations.
21. B. Hapke, *Theory of Reflectance and Emittance Spectroscopy* (Cambridge Univ. Press, New York, 1993).
22. J. R. Johnson *et al.*, *J. Geophys. Res.* **104**, 8809 (1999).
23. T. B. McCord *et al.*, *J. Geophys. Res.* **87**, 3021 (1982).
24. J. F. Bell III *et al.*, *J. Geophys. Res.* **102**, 9109 (1997).
25. R. V. Morris *et al.*, *J. Geophys. Res.* **94**, 2760 (1989).
26. R. V. Morris *et al.*, *J. Geophys. Res.* **105**, 1757 (2000).
27. M. B. Madsen *et al.*, *J. Geophys. Res.* **108**, 10.1029/2002JE002029 (2003).
28. H. Y. McSween *et al.*, *Science* **305**, 842 (2004).
29. Both pyroxene and olivine exhibit broad Fe^{2+} absorption bands centered near 900 to 1100 nm [e.g., (*30*, *31*)], but because the long-wavelength sides of these bands are typically beyond the spectral range of silicon CCD detectors, it is usually not possible to uniquely identify the specific Fe^{2+}-bearing phases responsible for reflectance decreases observed in the longest-wavelength filters of instruments such as Pancam.
30. J. B. Adams, *J. Geophys. Res.* **79**, 4829 (1974).
31. E. A. Cloutis *et al.*, *J. Geophys. Res.* **91**, 11641 (1986).
32. X. McSween *et al.*, *J. Geophys. Res.* **104,** 8679 (1999).
33. J. F. Bell III *et al.*, *Icarus* **158**, 56 (2002).
34. G. Klingelhöfer *et al.*, *Lunar Planet. Sci.* **XXXV**, abstr. 2184 (2004) [CD].
35. R. V. Morris *et al.*, *Science* **305**, 833 (2004)
36. M. Lemmon *et al.*, in preparation.
37. For example, M. J. Wolff *et al.*, *J. Geophys. Res.* **104,** 9027 (1999).
38. Meteor showers have been predicted to occur on Mars, e.g., (*41*).
39. J. F. Bell III, M. Lemmon, M. Wolff, *Transits of Mars I and II* (IAU Circular 8298, 8 March 2004)
40. J. F. Bell III *et al.*, in preparation.
41. F. Selsis *et al.*, *Astron. Astrophys.* **416,** 783 (2004).
42. We extend our sincere gratitude to the many hundreds of people who have contributed to the success of the Pancam investigation. These include the many MER engineers, managers, and support staffers at JPL; engineers and researchers at many vendor organizations; students and support staff at Cornell University, U.S. Geological Survey Flagstaff, Washington University, and other institutions; image processing and visualization experts at JPL and NASA Ames Research Center; and many of the co-investigators, collaborators, and associates on the Athena Science Team. The authors also extend special thanks to our families and loved ones for their patience and support during mission operations and throughout the many years leading up to Spirit's spectacular travels on Mars.

Plates Referenced in Article

www.sciencemag.org/cgi/content/full/305/5685/800/DC1
Plates 1 to 4 and 7 to 10

1 May 2004; accepted 16 July 2004